ACS OMEGA

http://pubs.acs.org/journal/acsodf

Article

Ni/Graphene Coating for Enhanced Corrosion Resistance of Metal Foam Flow Field in Simulated PEMFC Cathode Environment

Chuanfu Sun, Guilin Hu, Lili Cao, Taijun Pan, Chengfeng Guo, and Yuzhen Xia*

Cite This: *ACS Omega* 2024, 9, 29797−29804

Read Online

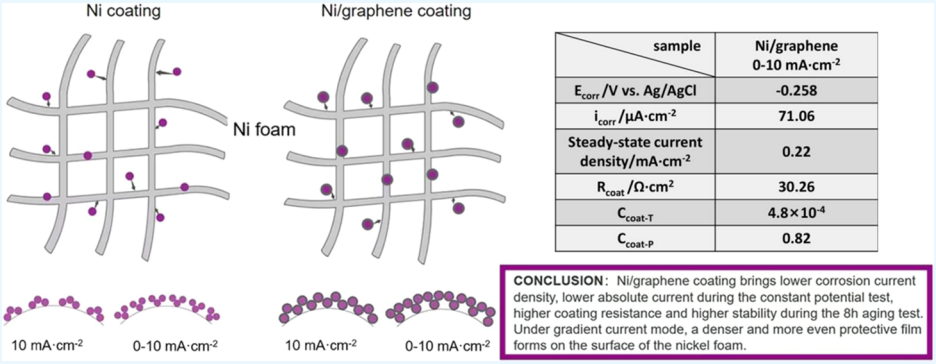

ABSTRACT: Metal foam flow field suffers serious corrosion issues in proton exchange membrane fuel cells due to its large surface area. Ni and Ni/graphene coatings are prepared under constant and gradient current modes, respectively, to improve the corrosion resistance. The effect of the electrodeposition current mode and the deposition mechanism is studied. Compared with Ni coating, Ni/graphene coating brings low corrosion current density and high coating resistance, effectively enhancing the stability of Ni foam in an acidic environment. Different from Ni coating with a single layer, Ni/graphene deposits have core−shell structure, with graphene coated on the surface of Ni nanoparticles. It is shown that graphene deposits cover the Ni particles during the electrodeposition, which protects nickel particles from agglomeration and forms an inert film on the surface of the porous structure. After an 8 h constant potential test, no significant pitting is observed on the surface of Ni/graphene coating, showing excellent anticorrosion performance. As to the effect of the deposition current mode, it is shown that more composite particles deposit on the upper layer under the gradient current mode, which brings denser protective film and fewer surface defects on the surface. Ni/graphene coating electrodeposited under a gradient current mode between 0 and 10 mA·cm^{-2} exhibits the lowest corrosion current densities. The values at 50 and 80 °C are only 62.9 and 26.0% of those of uncoated Ni foam, respectively.

1. INTRODUCTION

The proton exchange membrane fuel cell (PEMFC), with a proton exchange membrane (PEM) as the electrolyte, converts hydrogen and oxygen into electrical energy directly and produces only water through the redox reaction.[1,2] Owing to its high efficiency, quick start, high energy density, small size, and weight, it has become one of the most popular fuel cells and potential power sources for transportation, domestic power, and portable devices.[3,4] The most promising application for PEMFC is in fuel cell vehicles (FCVs), while the large-scale commercialization of FCVs put forward high requirements of PEMFC stacks, such as lower cost, higher performance, and durability. The stack power density of the latest Toyota FCV, the second-generation MIRAI launched at the end of 2020, is 4.4 KWl^{-1}, which is still far from the 2030 and 2040 targets announced by Japan's New Energy and Industrial Technology Development Organization for automotive applications, 6.0 and 9.0 kWl^{-1}, respectively.[5]

The core components of PEMFC contain membrane electrode assembly (MEA) and bipolar plate (BP).[6] BP with flow filed on each side plays a key role in distributing reaction gases, passing electricity, and separating every single cell, accounting for 80−85% of the total weight and 38% of the total cost.[7] Therefore, much attention has been paid to material modification and structure optimization of flow fields. Conventional flow fields, such as the parallel and serpentine ones, have been adopted since the early stage of fuel cell development.[8] Compared with the traditional rib-channel flow

Received: April 11, 2024
Revised: June 3, 2024
Accepted: June 4, 2024
Published: June 24, 2024

https://doi.org/10.1021/acsomega.4c03523
ACS Omega 2024, 9, 29797−29804

fields, the porous metal foam was used because of its lightweight feature to reduce the weight of fuel cell stacks.[9] Shen et al.[10] found that the introduction of metal foam could achieve a 44% decrease in thermal resistance compared with the composite material without metal foam. Tsai et al.[11] compared the use of metal foam and graphite bipolar plates as flow distributors in PEMFC. The results showed that the ohmic resistance, activation resistance, and mass transfer resistance were reduced as metal foam was used. Tseng et al.[12] found that the mass transport limitation was reduced because of the highly porous structure of metal foam, which also enabled the fuel cell with high tolerance to low cell temperature (40 °C) and low humidification. The porous metal foam with high porosity used for the flow field could promote the supply of gas reactants and the uniformity of gas distribution.[13,14] Moreover, the porous structure could improve the uniformity of the stress distribution on the contact surface, thereby improving the performance of the cells.[15]

In PEMFC, the components work under an acidic environment, with pH in the range of 2−4, and operational temperature around 80 °C, which suffer severe corrosion, especially for metal materials. The metallic BP forms a passive film and contributes to a high interfacial contact resistance in PEMFC.[16−18] Meanwhile, the corrosion products would pollute PEM and catalysts, hindering the performance and lifespan of fuel cells.[19] Compared with metal plates, metal foam is more prone to face more serious corrosion problems in PEMFC environments due to its larger surface area and being damaged from inside to outside. Surface coating technology has been widely used to solve the corrosive problems of metallic BP in fuel cells.[13,20] The protective layer can not only prevent the rapid oxidation of metal materials under high temperature and high humidity conditions but also enhance the conductivity of BP. Similar treatments have also been applied to enhance the performance of the metal foam flow field.[12]

The common surface modification methods include vapor deposition methods, electrodeposition, and so on.[21−25] Among those, the electrochemical deposition method has the advantage of simple, low-cost, and high deposition rates, which can be performed at ambient temperature and low pressure.[26,27] Liu et al.[28] prepared Cu−Ni coating using electrodeposition, which exhibited lower corrosion current density, higher corrosion potential, and larger impedance modulus, corresponding to higher corrosion resistance. Li et al.[29] prepared Ni−W/ZrO_2 nanocrystalline film by pulse electrodeposition to enhance the anticorrosion performance. Wang et al.[30] electrodeposited Ni/Sn coating on the surface of nickel metal foam. Both of the corrosion current densities at 50 and 80 °C were reduced by half because of Ni/Sn coating obtained under gradient current. Electrodeposited metal coatings could enhance the corrosion resistance of material surfaces, particularly when inert particles are incorporated, further enhancing this performance.[31,32]

Graphene, composed of carbon atom layers, has been widely applied in anticorrosion fields, due to its chemical stability and excellent conductivity.[29,30,33] Kumar et al.[31] prepared Ni-graphene composite coatings for anticorrosion applications on low-carbon steel matrix. The experiments in 3.5 wt % NaCl indicated that the addition of graphene resulted in a more compact coating structure and improved corrosion resistance. Yasin et al.[32] utilized the electrochemical codeposition technique to prepare Ni/graphene nanocomposite coatings on the surface of low-carbon steel using different current densities. Experimental results showed that the sample with a current density of 9 A·dm^{-2} exhibited the best corrosion resistance in a 3.5 wt % NaCl environment. Jiang et al.[34] studied the codeposition of graphene platelets and nickel composite coatings on carbon steel by electrodeposition process. The corrosion current density in 3.5 wt % NaCl was three times lower than that of mild steel. The anticorrosion ability of graphene coating was also demonstrated in the application onto the porous metal. Lee et al.[35] grew graphene on foam nickel surfaces using the chemical vapor deposition method. Tafel tests, in an H_2SO_4 environment with a pH of 3, showed that the corrosion current density of the samples coated with graphene was 9 times lower than that of bare foam nickel. Sim et al.[36] fabricated multilayer graphene-coated nickel foam by a rapid thermal annealing (RTA) system. The corrosion rate was reduced by 2 orders of magnitude in the working environment of H_2SO_4 (pH 1−1.5) with 2 ppm of HF.

Owing to its excellent conductivity and superior mass transfer performance, metal foam nickel is an ideal porous material for flow field applications. To overcome the serious corrosion problem in the PEMFC environment, we prepared graphene coatings onto the surface of the porous structure in this study. For well-distributed deposition of coating particles onto the metal foam, the electrodeposition method is applied in this study, with graphene coating obtained by codepositing in Ni solution with Ni particles. The Ni/graphene composite coating contains a double layer with inert graphene on the upper layer. Their corrosion resistance and electrodeposition mechanism are studied.

2. EXPERIMENTAL SECTION

2.1. Electrodeposition. The nickel foam was obtained from Kunshan Lvchuang Electronic Technology Co., Ltd. The thickness was 1 mm, and the pore diameter was around 600 μm. Before the electrodeposition, Ni foam was pretreated and activated in the 300 mL solution consisting of 35 g/L NaOH, 20 g/L Na_2CO_3, and 15 g/L $Na_3PO_4{\cdot}12H_2O$, for 20 min.[37] After that, the pretreated Ni foam was rinsed with deionized water and then dried in a 60 °C oven for 8 h. The Ni electrodeposition was carried out in the electrolyte 500 mL solution composed of 300 g·L^{-1} $NiSO_4{\cdot}6H_2O$, 45 g·L^{-1} $NiCl_2{\cdot}6H_2O$, 40 g·L^{-1} H_3BO_3, and 0.05 g·L^{-1} $C_{12}H_{25}SO_4Na$. The electroplating solution of Ni/graphene coatings was composed of 12.9 g·L^{-1} $Ni(SO_3NH_2)_2$, 9.51 g·L^{-1} $NiCl_2{\cdot}6H_2O$, 40 g·L^{-1} H_3BO_3, 0.05 g·L^{-1} $C_{12}H_{25}SO_4Na$, 10 g·L^{-1} $C_6H_5Na_3O_7$, 0.048 g·L^{-1} graphene (97 wt %), and 100 mL·L^{-1} C_5H_9NO (NMP). The required graphene was dispersed in 50 mL of NMP and then mixed with other components. All chemicals for the solution were purchased from Shanghai Macklin Biochemical Technology Co., Ltd.

The electrodeposition was carried out in a three-electrode system, with Ni foam as the cathode and nickel plate (99.9%, Chenshuo Co., Ltd., China) as the anode. The different current modes were operated on a CHI660E (Chenhua Co., Ltd., China). The temperature for electrodeposition was 328 K and the operation time was 20 min. The samples coated with nickel were named Ni10 (obtained at 10 mA·cm^{-2}) and Ni0-10 (obtained at 0−10 mA·cm^{-2}), and the nickel/graphene composites electrodeposited samples were named Ni/G10

https://doi.org/10.1021/acsomega.4c03523
ACS Omega 2024, 9, 29797−29804

(obtained at 10 mA·cm^{-2}) and Ni/G0-10 (obtained at 0−10 mA·cm^{-2}), respectively.

2.2. Morphology Investigation. X-ray diffraction (XRD) was carried out on KYOWAGLAS-XA H-12 (Kuraray Co., Ltd., Japan), using Cu Kα radiation, operated at 40 mA and 40 kV, with 2θ ranging from 5° to 80°, and a scanning speed at 0.04°·s^{-1}.

The Raman spectra were performed on a Horiba LabRAM HR Evolution Raman microscope (HORIBA Jobin Yvon, Japan) using green (532 nm) laser excitation. The spectral range 1000−3000 cm^{-1} was tested.

Scanning electron microscopy (SEM) was used to obtain the surface morphology on a Phenom ProX (Shanghai Phenom Scientific Co., Ltd., China) at 15 kV.

2.3. Corrosion Resistance Measurements. The electrochemical experiments were conducted using a CHI660E electrochemical workstation. In the three-electrode system, the working electrode is a piece of nickel foam with an area of 1 cm^2, with a Ag/AgCl electrode as the reference electrode and a platinum foil as the counter electrode.[38,39] Dynamic potential testing was performed in an H_2SO_4 solution with a pH of 3, within the range of −1.0−0.5 V vs Ag/AgCl, at a scan rate of 1 mV/s. The constant potential test was carried out at 0.6 V, with air purging into the H_2SO_4 solution with a pH of 3 to simulate the cathodic environment. Electrochemical impedance spectroscopy (EIS) tests were conducted at 50 and 80 °C in a 0.5 mol/L H_2SO_4 solution containing 2 ppm of HF. The frequency ranged from 10 kHz to 0.1 Hz, with an amplitude voltage of 10 mV applied at open-circuit potential.

3. RESULTS AND DISCUSSION

3.1. XRD Analysis. The XRD patterns of the Ni coating and Ni/graphene coating are shown in Figure 1. The XRD diffraction peaks at 44.56, 51.92, and 76.44° are related to the lattice planes of Ni (111), Ni (200), and Ni (220), respectively, which fit well with the reference spectra of face-centered cubic nickel. No obvious peak shift is depicted because of graphene coating. The diffraction peak at 26.50° is also observed in the patterns with a graphene coating, corresponding to a lattice fringe of 0.34 nm, which can be indexed to C (002).[40,41]

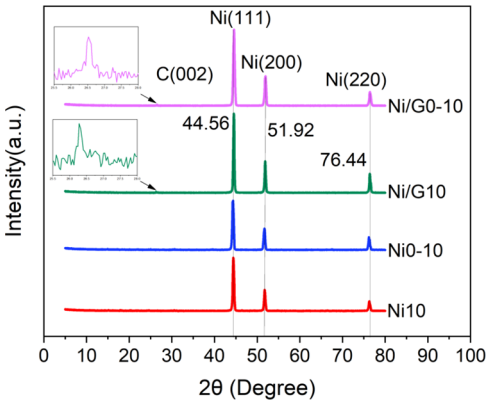

Figure 1. XRD patterns of Ni and Ni/graphene coatings.

The peak strength is enhanced due to the introduction of graphene, especially that of the Ni (111) peak. According to the analysis in the literature,[40] the graphene in the coating may change the growth orientation of Ni from (200) and (220) to (111).

The grain sizes of the nanoparticle deposits are calculated using the Debye Scherrer equation.[42]

$$L = \left(\frac{K\lambda}{\beta\cos\theta}\right)$$

In the equation, L represents the average grain size, K is the Scherrer constant, equal to 0.9, λ is the wavelength, equal to 0.15 nm, β is the full width at half-maximum of the diffraction peak, and θ is the diffraction angle (rad).

The values of L are shown in Table 1. For the same type of coating, the average grain size obtained at electroplating under a gradient current is smaller than that obtained at constant current electroplating. The addition of graphene further reduced the average grain size. During the electroplating process of composite materials, graphene enhances nucleation by forming a disordered arrangement in the matrix or diffusing on the surface toward the growth center of graphene. This mechanism of increasing nucleation and hindering the growth of composite material crystals leads to a reduction in grain size.[42]

Table 1. Grain Sizes of Ni and Ni/Graphene Composite Coatings

samples	Ni10	Ni0-10	Ni/G10	Ni/G0-10
grain sizes/nm	24.05	21.21	19.59	16.69

3.2. Raman Analysis. Raman spectroscopy is an effective tool for studying disorders and defects in carbon materials. So we use it to verify the presence of graphene and explore the degree of defects in the graphene arrangement in the coating. The Raman spectra of electrodeposited Ni/Graphene coating are shown in Figure 2. The characteristic spectra of the D and G bands are detected at 1359.26 and 1583.05 cm^{-1}, respectively. Meanwhile, a distinct and symmetrical 2D peak appeared at 2714.99 cm^{-1}. While the D peak is related to the breathing mode of sp^2 atoms in the ring, the G peak originates from the in-plane stretching vibration of sp^2-bonded carbon atoms. The ratio of I(D)/I(G), equal to the relative intensity between the D and G peaks, represents the integrity of graphene, while a higher ratio is related to a higher defect density.[43] The I(D)/I(G) ratio of Ni/G10 is 0.22, while the value of Ni/G0-10 is 0.27, indicating a higher graphene defect

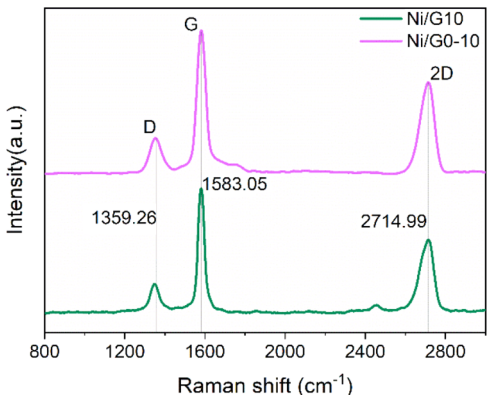

Figure 2. Raman spectra of Ni/graphene coating.

https://doi.org/10.1021/acsomega.4c03523
ACS Omega 2024, 9, 29797−29804

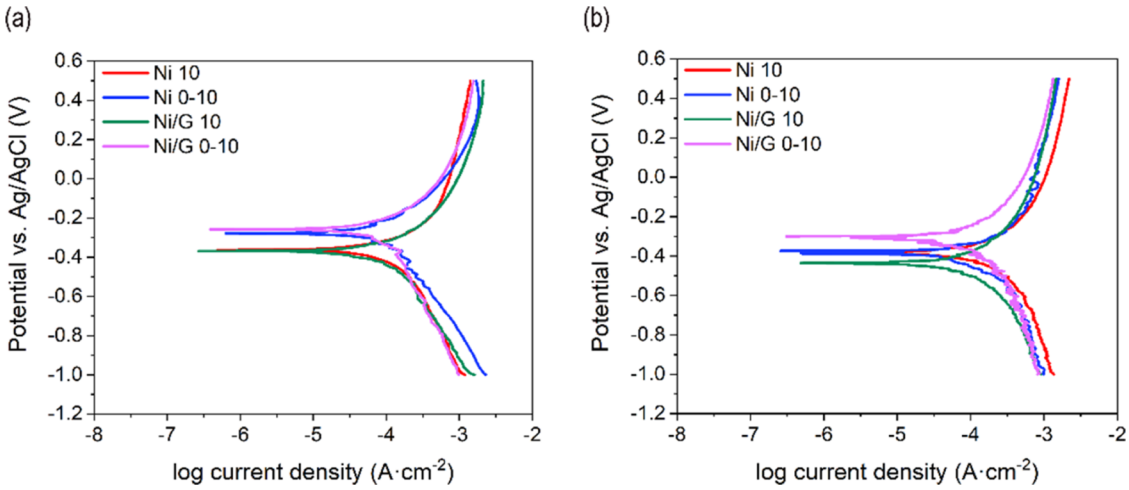

Figure 3. Tafel curves of Ni and Ni/graphene coating tested at 50 °C (a) and 80 °C (b).

Table 2. Electrochemical Parameters of Ni and Ni/Graphene Coatings Tested at 50 and 80 °C

electrochemical parameters	temperature (°C)	Ni10	Ni0-10	Ni/G10	Ni/G0-10
E_{corr} (V vs Ag/AgCl)	50	−0.363	−0.278	−0.368	−0.258
	80	−0.382	−0.367	−0.436	−0.302
i_{corr} (μA·cm^{-2})	50	93.06	92.70	72.33	71.06
	80	109.50	84.53	75.72	45.54
β_a (mV·dec^{-1})	50	5.381	5.689	5.249	5.788
	80	4.833	6.034	4.327	5.465
β_c (mV·dec^{-1})	50	4.395	3.270	4.671	5.987
	80	4.203	4.472	4.552	3.547
v_{corr} (×10^{-2} mm·y^{-1})	50	10.0	10.0	7.8	7.6
	80	11.8	9.1	8.1	4.9

density on its surface. The 2D peak, generated by a two-photon double resonance process, is used to evaluate the number of graphene layers prepared. A higher ratio of I(2D)/I(G) is explained by fewer graphene layers.[44] The ratios of Ni/G10 and Ni/G0-10 samples are 0.59 and 0.64, respectively, which may be due to the disordered distribution of multilayer graphene on the surface.[45]

3.3. Tafel Analysis. The Tafel curves of Ni and Ni/graphene coatings are tested in sulfuric acid with a pH of 3 at 50 and 80 °C, respectively, as shown in Figure 3. The corrosion potential (E_{corr}), corrosion current density (i_{corr}), anodic slope (β_a), cathodic slope (β_c) values, and corrosion rate (v_{corr}), obtained from Tafel analysis, are presented in Table 2[46,47] E_{corr} is a thermodynamic parameter represented by the intersection of the anodic polarization curve and the cathodic polarization curve in the graph. i_{corr} is a kinetic parameter, and its value is obtained through the Tafel extrapolation method from the polarization curve.[44] The values of β_a and β_c are also obtained using the same method.[48] β_a represents the influence of the activation energy of reactants on the reaction rate, wherein a higher value indicates a slower reaction rate. β_c represents the reduction rate of reactants on the electrode, and a lower value indicates a slower reaction rate.[49] v_{corr} can be determined based on the corrosion current using the corrosion rate formula.

The value of E_{corr} decreased with the testing temperature, indicating a higher possibility of a corrosion reaction at a high temperature. Relatively, higher E_{corr} values were obtained by electrodepositing nano-coating at gradient current. Ni/G0−10 exhibits the highest E_{corr} at 50 and 80 °C, respectively, whose value was close to those of uncoated Ni foam, −0.246 and −0.294 V vs Ag/AgCl, presented in ref 30. The low value of Ni/G10 may be attributed to the uneven graphene deposition obtained at a constant current.[33] The value of i_{corr} is used to evaluate the rate at which corrosion behavior occurs.[50] Similar to E_{corr}, i_{corr} usually increases with temperature, while the value of the uncoated sample at 80 °C, 174.8 μA·cm^{-2}, is 1.5 times than that of 112.9 μA·cm^{-2} at 50 °C.[30] Both values at 50 and 80 °C are reduced because of Ni and Ni/graphene coating. Ni/G0-10 exhibits the lowest corrosion current, meaning the highest stability at various temperatures. Meanwhile, smaller i_{corr} values and slower corrosion rates are obtained by Ni0-10 and Ni/G0-10, indicating that coatings obtained by electroplating at gradient current have better anticorrosion ability.

3.4. Constant Potential Analysis. As shown in Figure 4, the constant potential performances of Ni and Ni/graphene coating, operated at 0.6 V vs Ag/AgCl and 50 °C, are compared. Within the first few minutes, the current rapidly reaches a steady state, indicating that the material undergoes a rapid self-repair process.[51] While the steady current of uncoated Ni foam depicted in Wang et al.'s work is 0.50 mA·cm^{-2}, the values of Ni coating, obtained at constant current and gradient current, respectively, are 0.48 and 0.36 mA·cm^{-2}. The values of Ni/graphene coating are both around 0.22 mA·cm^{-2}, indicating better corrosion resistance, which is consistent with the results obtained in the Tafel analysis.

3.4.1. EIS Analysis. Figure 5a presents the Nyquist plots and the equivalent circuit of Ni and Ni/graphene coating. All of the coatings exhibit semicircles in Nyquist plots, presenting the same corrosion mechanisms. Based on that, the Randles circuit

https://doi.org/10.1021/acsomega.4c03523
ACS Omega 2024, 9, 29797−29804

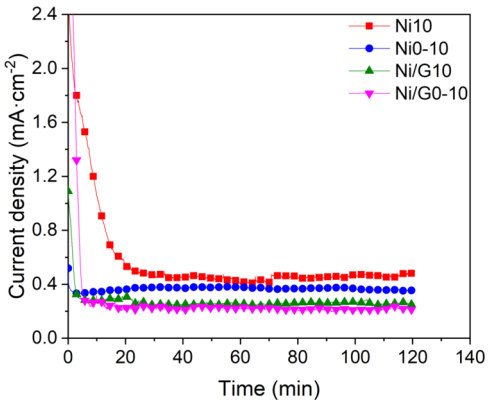

Figure 4. Constant potential curves of Ni and Ni/graphene electrodeposited porous nickel at various current densities.

is used as the equivalent circuit in this study, containing the solution resistance (R_s), constant-phase element capacitance (C_{coat}), and coating resistance (R_{coat}). The fitting results are listed in Table 3. All of the Nyquist plots start from the origin, as R_s is removed. Compared with the R_{coat} value of uncoated Ni foam, 5.27 Ω·cm^2, larger values are obtained after coating, which indicates better corrosion resistance.[52,53] The highest value is given by the sample Ni/G0−10.

Figure 5b,c is the Bode impedance plots in which the logarithm of the impedance (log(Z)) and the phase angle are plotted as a function of excitation frequency, respectively. The Bode plot contains three regions from high to low frequency, representing the corrosion occurring on the coating surface, inside the coating, and on the metal/coating interface, respectively.[54] As shown in Figure 5b, at a high-frequency range (10^2−10^4 Hz), the logarithmic amplitude plots appear flat. A slightly higher log(Z) is depicted by Ni/G0-10, indicating that this coating has the fewest surface defects. At the midfrequency range (10^1−10^2 Hz), the capacitive response of the coating system (C_{coat}) dominates, characterized by diagonal lines. As the frequency further decreases to the low-frequency range (10^{-1}−10^1 Hz), the coating resistance (R_{coat}) dominates, resulting in a flat log(Z) curve since resistance is frequency-independent.[53] In Figure 5c, the phase angle of the coated sample is around 40°, which could be attributed to the anticorrosion film coated on the surface of Ni foam.[55]

3.4.2. SEM Analysis. The stability of Ni and Ni/graphene coating is studied during the constant potential test at 0.6 V for 8 h. The microscopies before and after the test are shown in

Table 3. EIS Fitting Results of Ni and Ni/Graphene Coating

		C_{coat}		
i_{ed} (mA·cm^{-2})	R_s (Ω·cm^2)	$C_{coat\text{-}T}$	$C_{coat\text{-}P}$	R_{coat} (Ω·cm^2)
Ni10	5.52	8.3×10^{-3}	0.78	25.54
Ni0-10	5.36	4.8×10^{-3}	0.82	29.73
Ni/G10	4.76	5.5×10^{-3}	0.82	29.52
Ni/G0-10	5.36	4.8×10^{-4}	0.82	30.26

Figure 6. The surface morphologies shown in Figure 6a,b indicate that the deposition of Ni coating is mainly in particles. Comparatively, a more dense protective film is formed after electrodeposition at gradient current. The microstructures of Ni/graphene coating, shown in Figure 6c,d, indicate a smooth protective layer of graphene. Compared with the cracks, gaps, and voids found in the Ni coating, the deposits of Ni/graphene composite coating appear to be even and uniform, and no obvious aggregation is depicted. The graphene addition could cover the surface of nickel ions and hinder further growth during the electrodeposition. Meanwhile, more nucleation sites are offered for the reduction of nickel ions, and smaller and more uniform composite deposits are therefore obtained.[31,45]

In Figure 6e, the particle agglomeration phenomenon is shown on the surface of Ni10 after a constant potential test. Comparatively, a denser film forms on the surface of Ni0-10, without any apparent pitting corrosion, as depicted in Figure 6e. It may be attributed to the formation of an oxide film during the corrosion process. No obvious changes in the microscopies of Ni/G10 and Ni/G0-10 after 8 h are shown in Figure 6g,h, respectively. Compared with Ni/G10, the surface of Ni/G0-10 is flatter, and the distribution of graphene is more uniform and orderly. During the codeposition of Ni and graphene, graphene recovers the defects of Ni coating and protects the nanoparticles from corrosion and therefore attributes to better anticorrosion performance than Ni coating.[30]

To illustrate the deposition mechanisms of Ni and Ni/graphene coatings obtained under different modes, a schematic diagram is presented in Figure 7. Under the constant current mode, the particles are deposited onto the surface of Ni foam at a constant rate. It is important to control the current density and operation time to obtain a uniform and even coating. While insufficient coating results in pitting behavior, excess particle aggregation on the surface would cause more serious corrosion. With more particles depositing on the upper layer, the gradient current mode brings a denser protective film and

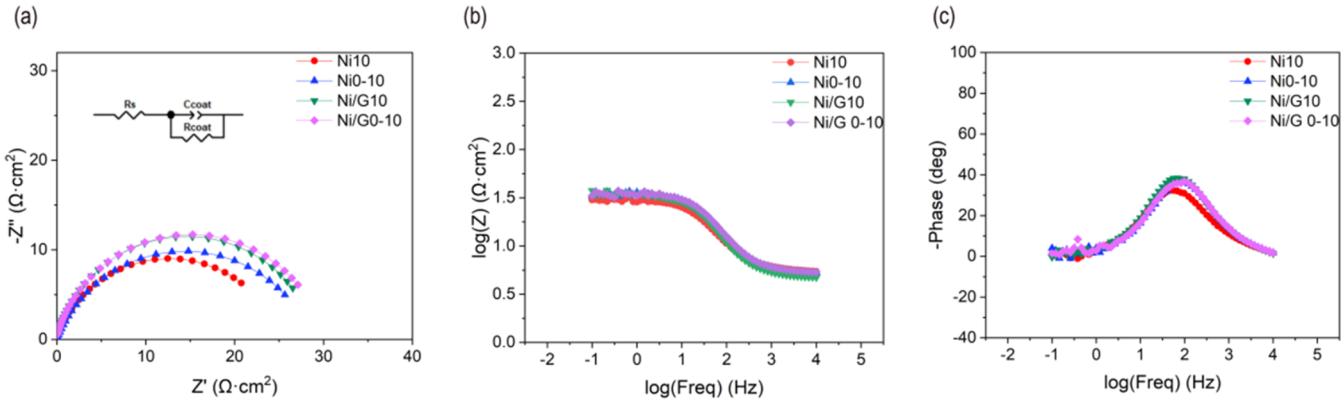

Figure 5. Nyquist impedance plots and equivalent circuit (a) and Bode impedance plots (b and c) of Ni and Ni/graphene coating.

https://doi.org/10.1021/acsomega.4c03523
ACS Omega 2024, 9, 29797−29804

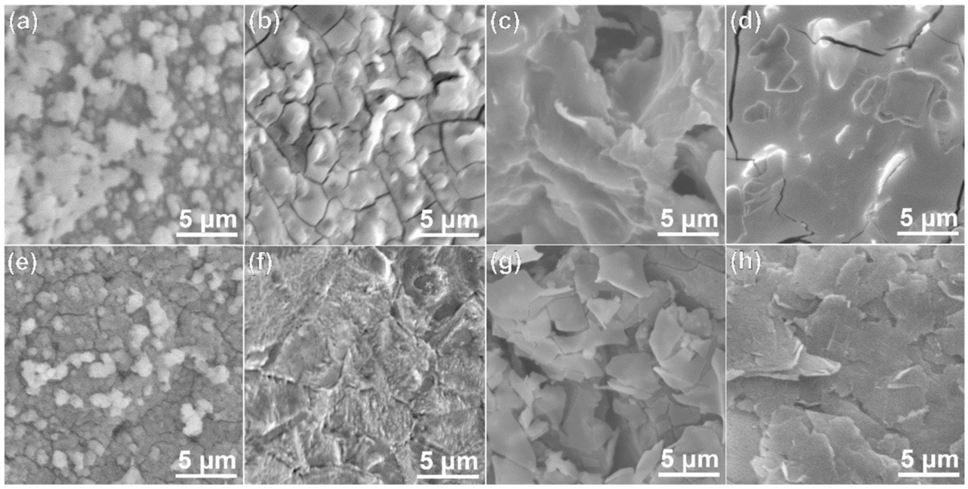

Figure 6. SEM images of Ni and Ni/graphene coating before (a−d) and after (e−h) 8 h constant potential test.

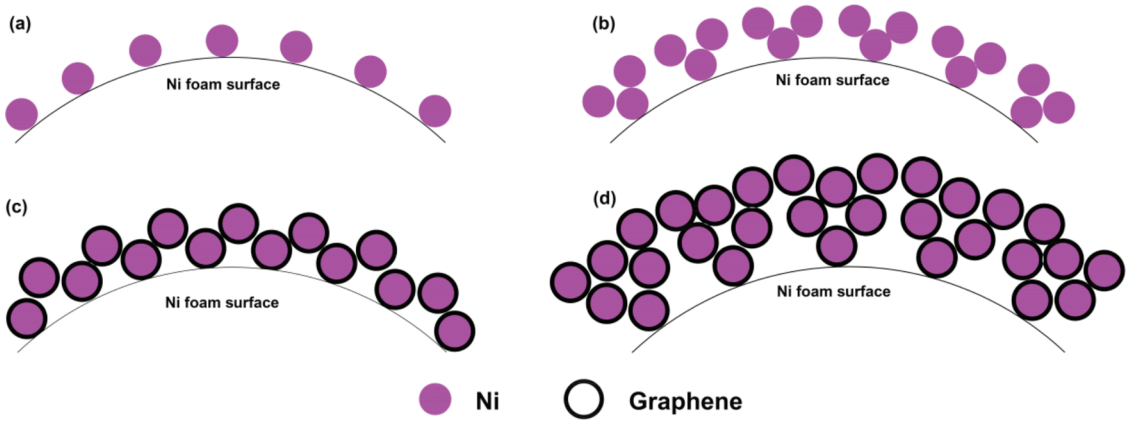

Figure 7. Deposition mechanisms of Ni10 (a), Ni0-10 (b), Ni/G10 (c), and Ni/G0-10 (d) on the surface of nickel foam.

fewer surface defects. With the addition of graphene, graphene covers the surface of the nickel particles, and the Ni/graphene coating with core−shell structure could protect them from aggregation and form a stable film on the porous structure.

4. CONCLUSIONS

In this study, Ni/graphene coatings with a core−shell structure are electrodeposited onto the surface of nickel foam to enhance the corrosion resistance. Moreover, the effect of graphene addition and the electrodeposition current mode is studied. The main conclusions can be drawn as follows:

(1) Compared with uncoated Ni foam, both Ni and Ni/graphene coatings bring lower corrosion current density, lower absolute current during the constant potential test, high coating resistance, and high stability during the 8 h aging test.

(2) While the electrodeposition of nickel is in particles, the presence of multilayer graphene diffusing on their surface hinders the growth of crystal size and forms an inert film on Ni foam.

(3) Under gradient current mode, a denser and more even protective film forms on the surface of the nickel foam, which contributes to the higher corrosion resistance of Ni0-10 and Ni/G0-10.

However, because of the low stability of metal foam, the value of i_{corr} is higher than the DOE requirement (1 μA·cm^{-2}) for bioplates. The application of the metal foam flow field requires more work to improve the corrosion resistance.

■ AUTHOR INFORMATION

Corresponding Author

Yuzhen Xia − *School of Mechanical and Energy Engineering, Zhejiang University of Science and Technology, Hangzhou 310023, China;* orcid.org/0000-0002-6779-8403; Email: yuzhen.xia@zust.edu.cn

Authors

Chuanfu Sun − *School of Mechanical and Energy Engineering, Zhejiang University of Science and Technology, Hangzhou 310023, China*

Guilin Hu − *School of Mechanical and Energy Engineering, Zhejiang University of Science and Technology, Hangzhou 310023, China;* orcid.org/0000-0001-6703-9135

Lili Cao − *School of Mechanical and Energy Engineering, Zhejiang University of Science and Technology, Hangzhou 310023, China*

Taijun Pan − *School of Mechanical and Energy Engineering, Zhejiang University of Science and Technology, Hangzhou 310023, China*

Chengfeng Guo − *School of Mechanical and Energy Engineering, Zhejiang University of Science and Technology, Hangzhou 310023, China*

Complete contact information is available at:

https://doi.org/10.1021/acsomega.4c03523
ACS Omega 2024, 9, 29797−29804

https://pubs.acs.org/10.1021/acsomega.4c03523

Notes

The authors declare no competing financial interest.

■ ACKNOWLEDGMENTS

The authors acknowledge the financial support of research start-up funds and the Graduate Innovation Fund (No. 2023y jskc03) from the Zhejiang University of Science and Technology, China.

■ REFERENCES

(1) Gou, Y.; Jiang, G.; Hao, J.; Shao, Z.; Wei, Z. A corrosion mechanism of NbC/alpha-C:H films for metallic bipolar plates in proton exchange membrane fuel cell cathode based on percolation model. *Surf. Coat. Technol.* **2022**, *445*, No. 128711.

(2) Abdel-Basset, M.; Mohamed, R.; Abouhawwash, M. On the facile and accurate determination of the highly accurate recent methods to optimize the parameters of different fuel cells: Simulations and analysis. *Energy.* **2023**, *272*, No. 127083.

(3) Tan, Q.; Wang, Y. Preparation and properties of conductive Ti4O7 surface coating for Ti bipolar plates of proton exchange membrane fuel cells. *J. Alloys Compd.* **2022**, *911*, No. 165098.

(4) Zhang, G.; Qu, Z.; Tao, W.; Wang, X.; Wu, L.; Wu, S.; Xie, X.; Tongsh, C.; Huo, W.; Bao, Z.; Jiao, K.; Wang, Y. Porous Flow Field for Next-Generation Proton Exchange Membrane Fuel Cells: Materials, Characterization, Design, and Challenges. *Chem. Rev.* **2023**, *123*, 989−1039.

(5) Jiao, K.; Xuan, J.; Du, Q.; Bao, Z.; Xie, B.; Wang, B.; Zhao, Y.; Fan, L.; Wang, H.; Hou, Z.; Hou, S.; Brandon, N. P.; Yin, Y.; Guiver, M. D. Designing the next generation of proton-exchange membrane fuel cells. *Nature* **2021**, *595*, 361−369.

(6) Zhang, C.; Ma, J.; Liang, X.; Luo, F.; Cheng, R.; Gong, F. Fabrication of metallic bipolar plate for proton exchange membrane fuel cells by using polymer powder medium based flexible forming. *J. Mater. Process Technol.* **2018**, *262*, 32−40.

(7) Wang, Y.; Tan, Q.; Huang, B. Synthesis and properties of novel N/Ta-co-doped TiO2 coating on titanium in simulated PEMFC environment. *J. Alloys Compd.* **2021**, *879*, No. 160470.

(8) Lu, J.; Xia, Y.; Hu, Y.; Wang, Z.; Lei, H.; Hu, G. Study on transport phenomena and performance of proton exchange membrane fuel cell with radial flow fields. *Eng. Appl. Comput. Fluid Mech.* **2023**, *17*, No. e2156925.

(9) Zhang, Y.; Chen, B.; Meng, K.; Zhou, H.; Chen, W.; Zhang, N.; Deng, Q.; Yang, G.; Tu, Z. Optimal design of a cathode flow field for performance enhancement of PEM fuel cell. *Appl. Energy.* **2023**, *343*, No. 121226.

(10) Shen, B.; Yan, H.; Sunden, B.; Xue, H.; Xie, G. Forced convection and heat transfer of water-cooled microchannel heat sinks with various structured metal foams. *Int. J. Heat Mass Transfer* **2017**, *113*, 1043−1053.

(11) Tsai, B.-T.; Tseng, C.; Liu, Z.; Wang, C.; Lee, C.; Yang, C.; Lo, S. Effects of flow field design on the performance of a PEM fuel cell with metal foam as the flow distributor. *Int. J. Hydrogen Energy* **2012**, *37*, 13060−13066.

(12) Tseng, C.-J.; Tsai, B. T.; Liu, Z.; Cheng, T.; Chang, W.; Lo, S. A PEM fuel cell with metal foam as flow distributor. *Energy Convers. Manage.* **2012**, *62*, 14−21.

(13) Kumar, A.; Reddy, R. Materials and design development for bipolar/end plates in fuel cells. *J. Power Sources* **2004**, *129*, 62−67.

(14) Vazifeshenas, Y.; Sedighi, K.; Shakeri, M. Heat transfer in PEM cooling flow field with high porosity metal foam insert. *Appl. Therm. Eng.* **2019**, *147*, 81−89.

(15) Chen, X.; Yang, C.; Sun, Y.; Liu, Q.; Wan, Z.; Kong, Z.; Tu, Z.; Wang, X. Water management and structure optimization study of nickel metal foam as flow distributors in proton exchange membrane fuel cell. *Appl. Energy.* **2022**, *309*, No. 118448.

(16) Jiang, L.; Syed, J.; Lu, H.; Meng, X. In-situ electrodeposition of conductive polypyrrole-graphene oxide composite coating for corrosion protection of 304SS bipolar plates. *J. Alloys Compd.* **2019**, *770*, 35−47.

(17) Bian, H.; Zhang, G.; Zhai, Q.; Du, Y.; Ma, Y.; Yang, B.; Tang, S.; Bin, D.; Meng, X.; Lu, H. Enhanced corrosion resistance by polypyrrole and Ti3C2Tx-acrylic epoxy double-layer coating for 304SS bipolar plates of PEMFC. *J. Ind. Eng. Chem.* **2023**, *122*, 520−528.

(18) Jiang, L.; Syed, J.; Gao, Y.; Zhang, Q.; Zhao, J.; Lu, H.; Meng, X. Electropolymerization of camphorsulfonic acid doped conductive polypyrrole anti-corrosive coating for 304SS bipolar plates. *Appl. Surf. Sci.* **2017**, *426*, 87−98.

(19) Joseph, S.; McClure, J.; Sebastian, P.; Moreira, J.; Valenzuela, E. Polyaniline and polypyrrole coatings on aluminum for PEM fuel cell bipolar plates. *J. Power Sources* **2008**, *177*, 161−166.

(20) Li, T.; Zhang, H.; Wang, Y.; Wu, C.; Yan, Y.; Chen, Y. TiCr transition layer promoting the growth of high-stability TiCrN coating for titanium bipolar plate. *Surf. Coat. Technol.* **2022**, *451*, No. 129026.

(21) Zhu, W.; Gao, H.; Zheng, F.; Huang, T.; Wu, F.; Wang, H. Electrodeposition of graphene by cyclic voltammetry on nickel electrodes for microbial fuel cells applications. *Int. J. Energy Res.* **2019**, *43*, 2795−2805.

(22) Bai, H. H.; Maxwell, T. L.; Kordesch, M. E.; Balk, T. J. Physical vapor deposition and thermally induced faceting of tungsten nanoparticles. *Mater. Charact.* **2023**, *198*, No. 112724.

(23) Satpathy, B.; Kayal, N.; Jena, S.; Das, S.; Das, K. Structural and mechanical characterization of nano-structured Cu-Ag bimetallic coatings developed from a novel thiourea-based electroplating bath. *Mater. Charact.* **2022**, *189*, No. 112011.

(24) Li, J.; Lin, O.; Cheng, C.; Wang, W.; Xu, C.; Ren, L. Fabrication of a Ni/SiC composite coating on steel surface with excellent corrosion inhibition performance. *J. Mater. Process. Technol.* **2021**, *290*, No. 116987.

(25) Cheng, R.; Luo, X.; Huang, G.; Li, C. Corrosion and wear resistant WC17Co-TC4 composite coatings with fully dense microstructure enabled by in-situ forging of the large-sized WC17Co particles in cold spray. *J. Mater. Process. Technol.* **2021**, *296*, No. 117231.

(26) Song, Y.-J.; Kim, J.; Park, K. Synthesis of Pd Dendritic Nanowires by Electrochemical Deposition. *Cryst. Growth Des.* **2009**, *9*, 505−507.

(27) Bian, H.; Du, Y.; Ren, Y.; Wu, H.; Wu, Y.; Ma, Y.; Yang, B.; Tang, S.; Bin, D.; Lu, H.; Meng, X. One-step electrodeposition of polypyrrole/Ti3C2Tx MXene composite coating for 304SS bipolar plates in PEMFC. *Surf. Coat. Technol.* **2023**, *462*, No. 129460.

(28) Liu, E.; Yin, X.; Hu, J.; Yu, S.; Zhao, Y.; Xiong, W. Fabrication of a biomimetic hierarchical superhydrophobic Cu-Ni coating with self-cleaning and anti-corrosion properties. *Colloid Surface A* **2020**, *586*, No. 124223.

(29) Li, B.; Zhang, W.; Li, D.; Wang, J. Electrodeposition of Ni W/ZrO2 nanocrystalline film reinforced by CeO2 nanoparticles: Structure, surface properties and corrosion resistance. *Mater. Chem. Phys.* **2019**, *229*, 495−507.

(30) Wang, Z.; Xia, Y.; Lei, H.; Hu, G. Enhanced corrosion resistance of Ni/Sn nano-electrodeposited metal foam for flow field application in simulated PEMFC cathode environment. *Int. J. Hydrogen Energy* **2022**, *47*, 35412−35422.

(31) Kumar, C. M. P.; Venkatesha, T. V.; Shabadi, R. Preparation and corrosion behavior of Ni and Ni−graphene composite coatings. *Mater. Res. Bull.* **2013**, *48*, 1477−1483.

(32) Yasin, G.; Arif, M.; Shakeel, M.; Dun, Y.; Zuo, Y.; Khan, W. Q.; Tang, Y.; Khan, A.; Nadeem, M. Exploring the Nickel-Graphene Nanocomposite Coatings for Superior Corrosion Resistance: Manipulating the Effect of Deposition Current Density on its Morphology, Mechanical Properties, and Erosion-Corrosion Performance. *Adv. Eng. Mater.* **2018**, *20*, No. 1701166.

(33) Suranshe, S. S.; Patil, A.; Deshmukh, T.; Chavhan, J. One step electrode fabrication of thin film graphene oxide-polypyrrole

composite by electrodeposition using cyclic voltammetry for hybrid type supercapacitor application. *Electrochim. Acta* **2023**, *450*, No. 142277.
(34) Jiang, K.; Li, J.; Liu, J. Electrochemical codeposition of graphene platelets and nickel for improved corrosion resistant properties. *RSC Adv.* **2014**, *4*, 36245−36252.
(35) Lee, Y.-H.; Li, S.; Tseng, C.; Su, C.; Lin, S.; Jhuang, J. Graphene as corrosion protection for metal foam flow distributor in proton exchange membrane fuel cells. *Int. J. Hydrogen Energy* **2017**, *42*, 22201−22207.
(36) Sim, Y.; Kwak, J.; Kim, S.; Jo, Y.; Kim, S.; Kim, S.; Kim, J.; Lee, C.; Jo, J.; Kwon, S. Formation of 3D graphene-Ni foam heterostructures with enhanced performance and durability for bipolar plates in a polymer electrolyte membrane fuel cell. *J. Mater. Chem. A* **2018**, *6*, 1504−1512.
(37) Li, N.; Xu, H.; Li, X.; Chen, W.; Zheng, L.; Lu, L. Tribological Properties and Corrosion Resistance of Porous Structure Ni-Mo/ZrO2 Alloys. *Coatings* **2020**, *10*, 767.
(38) Saidi, R.; Ashrafizadeh, F.; Raeissi, K.; Kharaziha, M. Electrochemical aspects of zinc oxide electrodeposition on Ti6Al4V alloy. *Surf. Coat. Technol.* **2020**, *402*, No. 126297.
(39) Wang, L.; Li, L.; Liu, H.; Wang, S.; Fang, H.; Gao, H.; Gao, K.; Zhang, Y.; Sun, J.; Yan, J. Polylaminate TaN/Ta coating modified ferritic stainless steel bipolar plate for high temperature proton exchange membrane fuel cell. *J. Power Sources.* **2018**, *399*, 343−349.
(40) Yigit, O.; Dikici, B.; Senocak, T. C.; Ozdemir, N. One-step synthesis of nano-hydroxyapatite/graphene nanosheet hybrid coatings on Ti6Al4V alloys by hydrothermal method and their in-vitro corrosion responses. *Surf. Coat. Technol.* **2020**, *394*, No. 125858.
(41) Dehghani, Z.; Ostovari, F.; Sharifi, S. A comparison of the crystal structure and optical properties of reduced graphene oxide and aminated graphene nanosheets for optoelectronic device applications. *Optik.* **2023**, *274*, No. 170551.
(42) Khalid, N. B.; Sarwar, M.; Rakha, A.; Khalid, A.; Munawar, A.; Riaz, A.; Rehman, R.; Akhtar, S. Medicinal honeycomb ceria nanoparticles' fabrication by using green synthesis method. *Appl. Nanosci.* **2022**, *12*, 2933−2943.
(43) Lee, G. W.; Shim, G. H.; Kim, J. M.; Seol, C.; Kim, J. H.; Kim, S. M.; Ahn, H. S. Two/three-dimensional reduced graphene oxide coating for porous flow distributor in polymer electrolyte membrane fuel cell. *Int. J. Hydrogen Energy* **2020**, *45*, 12972−12981.
(44) Siddaiah, A.; Kumar, P.; Henderson, A.; Misra, M.; Menezes, P. L. Surface Energy and Tribology of Electrodeposited Ni and Ni−Graphene Coatings on Steel. *Lubricants* **2019**, *7*, 87.
(45) Li, X.; Shen, Q.; Zhang, Y.; Wang, L.; Nie, C. Wear behavior of electrodeposited nickel/graphene composite coating. *Diamond Relat. Mater.* **2021**, *119*, No. 108589.
(46) López-Ortega, A.; Arana, J.; Rodriguez, E.; Bayon, R. Corrosion, wear and tribocorrosion performance of a thermally sprayed aluminum coating modified by plasma electrolytic oxidation technique for offshore submerged components protection. *Corros. Sci.* **2018**, *143*, 258−280.
(47) Fu, Z.; Gao, G.; Zhu, Z.; Ma, C.; Wang, W.; Zhang, L.; Hu, Y.; Gao, W. Stress corrosion cracking behavior of SUS301L-MT stainless steel laser-arc hybrid welded joints. *Corros. Sci.* **2018**, *143*, 23−30.
(48) Bahtli, T.; Ozbay, N. S. Corrosion resistances of C30 concrete: Effect of finely ground bronze sawdust waste. *Mater. Chem. Phys.* **2020**, *243*, No. 122588.
(49) Rybalka, K. V.; Beketaeva, L. A.; Bukhan Ko, N. G.; Davydov, A. D. Electrochemical behavior and the rate of general corrosion of NiAl intermetallic compound in the unbuffered sodium chloride solutions. *Corros. Sci.* **2011**, *53*, 630−636.
(50) Ren, Y.; Wu, H.; Du, J.; Liu, B.; Wang, X.; Jiao, Z.; Tian, Y.; Baker, I. Effect of laser scanning speeds on microstructure, tribological and corrosion behavior of Ti-23Nb alloys produced by laser metal deposition. *Mater. Charact.* **2023**, *197*, No. 112647.
(51) Wang, H. Stainless steel as bipolar plate material for polymer electrolyte membrane fuel cells. *J. Power Sources* **2003**, *115*, 243−251.
(52) Qi, S.; Li, X.; Zhang, Z.; Dong, H. Fabrication and characterisation of electro-brush plated nickel-graphene oxide nano-composite coatings. *Thin Solid Films* **2017**, *644*, 106−114.
(53) Wu, W.; Chen, R.; Yang, Z.; He, Z.; Zhou, Y.; Lv, F. Corrosion resistance of 45 carbon steel enhanced by laser graphene-based coating. *Diamond Relat. Mater.* **2021**, *116*, No. 108370.
(54) Nam, N. D.; Kim, M. J.; Jo, D. S.; Kim, J. G.; Yoon, D. H. Corrosion protection of Ti/TiN, Cr/TiN, Ti/CrN, and Cr/CrN multi-coatings in simulated proton exchange membrane fuel cell environment. *Thin Solid Films* **2013**, *545*, 380−384.
(55) Bao, Z.; Wang, Y.; Jiao, K. Liquid droplet detachment and dispersion in metal foam flow field of polymer electrolyte membrane fuel cell. *J. Power Sources* **2020**, *480*, No. 229150.

https://doi.org/10.1021/acsomega.4c03523
ACS Omega 2024, 9, 29797−29804